



Visible-LED-light-driven photocatalytic synthesis of N-heterocycles mediated by a polyoxometalate-containing mesoporous zirconium metal-organic framework

Samireh Karamzadeh^a, Esmail Sanchooli^{a,*}, Ali Reza Oveisi^{a,*}, Saba Daliran^a, Rafael Luque^{b,c}

^a Department of Chemistry, University of Zabol, P.O. Box: 98615-538 Zabol, Iran

^b Departamento de Química Orgánica, Universidad de Córdoba, Campus de Rabanales, Edificio Marie Curie (C-3), Ctra Nnal IV-A, Km 396, E14014 Córdoba, Spain

^c Peoples Friendship University of Russia (RUDN University), 6 Miklukho-Maklaya Str., 117198 Moscow, Russia

ARTICLE INFO

Keywords:

Hantzsch 1,4-dihydropyridines
Pyridines
Porphyrinic metal-organic frameworks
Polyoxometalate
Nanoporous materials
Multifunctional catalyst
Multicomponent reaction
Photo-oxidation

ABSTRACT

A mesoporous metal-organic framework with photothermal properties, namely PCN-222, was solvothermally synthesized from *meso*-tetra(4-carboxyphenyl)porphyrin and zirconium chloride employing both benzoic acid (BA) and trifluoroacetic acid (TFA) as modifiers. The MOF material subsequently served as a porous support for a polyoxometalate (POM), $H_3PW_{12}O_{40}$, via a facile impregnation method which rendered a novel porous POM@PCN-222 composite. The solid was characterized by FT-IR, PXRD, SEM/EDX, TGA/DSC, ICP-OES, UV-Vis DRS, cyclic voltammetry (CV), and BET surface area. The one-pot synthesis of *N*-heterocycles (pyridine derivatives) was investigated utilizing the hybrid material via one-pot *pseudo* four-component reaction between aromatic aldehydes, methyl acetoacetate and ammonium acetate promoted under visible LED light irradiation in the presence of molecular oxygen as green oxidant. Products were selectively formed in good yields in the presence of the recyclable heterogeneous solid. Remarkably, POM@PCN-222 showed a superior performance for this procedure as compared to both unfunctionalized MOF and POM. The photosensitizer and photothermal properties of the porphyrin linkers combined with Lewis acidic sites derived from PW_{12} and Zr_6 -nodes were responsible for the observed excellent performance. To understand the mechanism, control investigations, electron paramagnetic resonance (EPR) analysis and FT-IR reaction monitoring were performed. The work discloses, for the first time, a simple and environmentally friendly approach for the direct production of pyridines via one-pot thermo-photocatalytic approach using a novel POM-modified MOF in the absence of any chemical additive.

1. Introduction

Metal-organic frameworks (MOFs) are predominantly three-dimensional (3D) periodic metal-node and organic-linker assemblies, having permanent porosity, structural tenability, low density and large specific surface area [1]. MOFs have recently attracted significant attention for promising applications in adsorption [2], catalysis [3], and others [4–6]. The well-ordered pillars of MOFs are ideal networks for molecular diffusion, separation or catalysis, being established as powerful platforms for the design of advanced functional materials in various applications [7]. However, the field of MOFs as heterogeneous photocatalysts [8,9], particularly for selective organic transformations, is largely unexplored [10]. Visible-light-triggered organic

transformations, compared to conventional synthetic methods, have most-valued benefits in the field of green chemistry and sustainable development [10,11].

Polyoxometalates (POMs), metal oxide polyanions, are primarily made of early-transition-metals linked by oxygen [12]. POMs have been reported for catalytic applications due to their versatile structures, acidity and redox capability, and oxygen-rich surface. However, POMs suffer from low specific area, and mainly, high solubility under reaction conditions which make them difficult for recovering and reusing. To overcome these disadvantages, MOFs as solid supports have most-commonly been employed to immobilize POMs [13–15]. As a result, Xie et al. encapsulated Keggin-type POMs/POM-based ionic liquids in carboxylated UiO-66, MIL-100(Fe) and magnetically separable

* Corresponding authors.

E-mail addresses: Esmail_sanchooli@uoz.ac.ir (E. Sanchooli), aroveisi@uoz.ac.ir (A.R. Oveisi).

<https://doi.org/10.1016/j.apcatb.2021.120815>

Received 1 August 2021; Received in revised form 30 September 2021; Accepted 9 October 2021

Available online 13 October 2021

0926-3373/© 2021 Published by Elsevier B.V.

ZIF-8 to improve both the activity and stability in heterogeneously catalyzed biodiesel production [16–18]. MIL-101 has also been employed to load POM (MIL-101/POM) as efficient catalyst in several reactions including alkene oxidations, esterifications, Knoevenagel and Baeyer condensations [19–22]. However, Alcañiz et al. reported that the ion exchange can occur between the two components [21], limiting the development and use of POM@MIL-101 composites. Farha and co-workers introduced a POM@mesoporous NU-1000 hybrid material which exhibited excellent catalytic activities in the oxidation of 2-chloroethyl ethyl sulfide in the presence of H_2O_2 [23]. Very recently, Fang et al., incorporated a typical POM in photothermal Zr-ferrocene (Zr-Fc) MOF nanosheets [24] to prepare a highly efficient catalyst for the cycloaddition of styrene oxide to CO_2 under simulated sunlight using TBAB as co-catalyst [25]. However, to the best of our knowledge, the family of POM@MOFs is not yet reported for a heterogeneous multi-component reaction in literature.

1,4-Dihydropyridines (1,4-DHPs) and pyridines are two most main classes of *N*-heterocyclic and potentially active structures found commonly in natural products and used in medical chemistry, pharmaceuticals, additives, organic synthesis, and industry [26,27]. Nifedipine, nicardipine, vitamin B₃, and vitamin B₆ are several bioactive compounds comprising these structures (Scheme 1).

A possible route for the preparation of pyridines is the oxidation of the corresponding 1,4-dihydropyridines. Classically, Hantzsch 1,4-dihydropyridines are synthesized *via* one-pot reaction between β -keto esters, aldehydes and ammonia source [28,29]. In nature, cytochrome P-450 enzymes are responsible for the oxidation and conversion of 1,4-dihydropyridines, as calcium channel blockers, to their corresponding pyridines [30,31].

A number of methodologies have been reported for the synthesis of pyridines [32] including the one-pot oxidation of 1,4-dihydropyridines using $(NH_4)_2Ce(NO_3)_6$ [33], pyridinium chlorochromate (PCC) [34], Pd/C in AcOH [35], *N*-hydroxyphthalimide/ $Co(OAc)_2$ [36], Triton-X-100/ $K_2S_2O_8$ /light irradiation ($\lambda > 300$ nm) [37], acetate buffer (pH 4.37)/laccase/ABTS (diammonium salt) [38], and gold nanoparticles supported on carbon nanotubes (AuCNT)/quinone [39]. These protocols are associated with main drawbacks including the use of stoichiometric/costly oxidant/catalysts, the use of additives and harsh

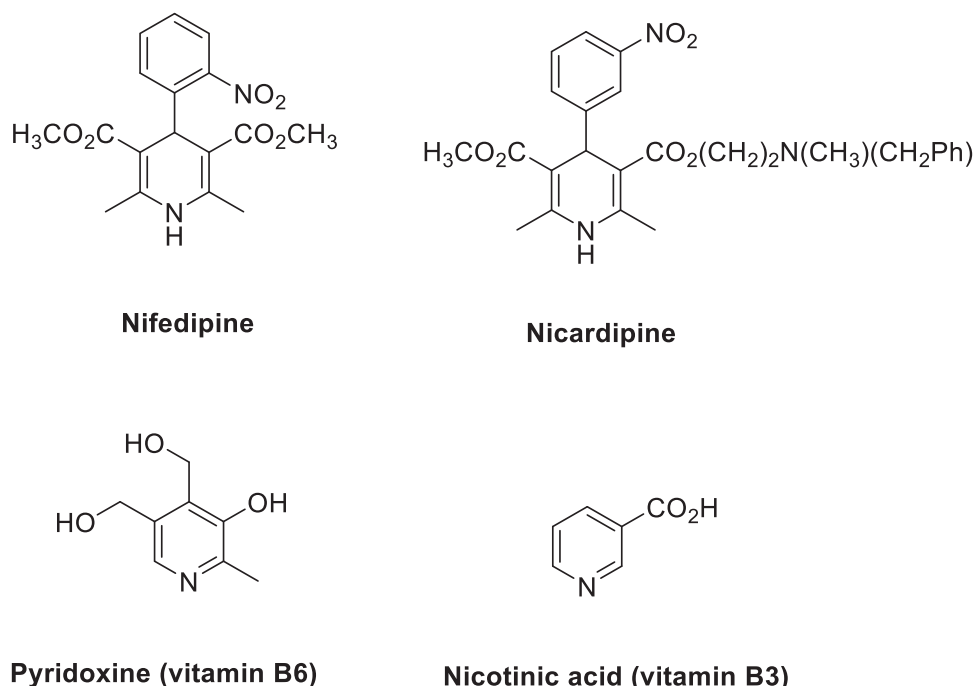
reaction conditions. Importantly, the synthesis and oxidation of 1,4-dihydropyridines in a one-pot fashion towards the formation of pyridines under mild reaction conditions is still challenging.

This report discloses the unprecedented design of a Keggin-type POM, $H_3PW_{12}O_{40}$, incorporated into mesoporous PCN-222 (PCN is Porous Coordination Network) [40,41] with photothermal properties, denoted here POM@PCN-222, as a highly efficient and reusable visible light (photo)catalyst for the direct synthesis of pyridine derivatives via one-pot *pseudo* four-component reaction utilizing O_2 as green oxidant. This composite can act both as a reusable catalyst and photocatalyst. PCN-222 [40,41] is a highly stable Zr-MOF with high surface area and well-defined mesoporosity, comprising tetracarboxylic free-base porphyrin (TCPP) linkers, as photosensitizer and photothermal component, and $Zr_6(\mu_3-O)_4(\mu_3-OH)_4(OH)_4(H_2O)_4$ nodes, as Lewis acid sites. In addition to the Zr-nodes on the MOF, as observed for NU-1000, amine moieties of TCPP allow a better interaction of PCN-222 with POM. MOFs having porphyrin moieties such as TCPP exhibit photothermal properties [42,43]. To the best of our knowledge, this is the first report on the use of such POM@MOF hybrid materials with photothermal performance and catalytic active sites in multicomponent reactions performed under visible-LED irradiation without the need of any additive, which can open new avenues for future industrial organic applications.

2. Experimental section

2.1. Materials and instruments

Chemicals were purchased from Merck and Sigma-Aldrich companies. 5,10,15,20-tetrakis(4-carboxyphenyl)porphyrin (TCPP) was synthesized via two-step synthetic process according to the method in the literature [41]. Free-base PCN-222 was prepared based on the reported synthetic procedure with minor changes [40], extending the reaction time to 24 h. UiO-66 ($Zr_6O_4(OH)_4(BDC)_4(Cl)_{0.4}(OH)_{3.6}(DMF)_2(EtOH)_{2.5}$) was prepared according to the previous method [44]. Scanning electron microscopy (SEM) images and energy dispersive X-ray spectroscopy (EDX) line scans were collected using a MIRA3 TESCAN, Czech Republic. Transmission electron microscopy (TEM) images were achieved from Tecnai™ G2 F20 series TEM. X-ray



Scheme 1. Some structures of bioactive 1,4-dihydropyridines and pyridines.

diffractometer (Philips Xpert, Netherlands) and Fourier transform infrared (FTIR) spectrometer (PerkinElmer, USA) were employed to characterize the synthesized nanocomposites. FT-IR monitoring of the reaction between methyl acetoacetate, benzaldehyde, and ammonium acetate for direct synthesis of corresponding pyridine were achieved from 4000 to 400 cm^{-1} and sampling intervals ranging from 30 min to 33 h (step 1: 30, 60, 120, 180, and 300 min followed by step 2: 4, 8, 12, 18, and 28 h). All samples were activated by heating at 120 °C for 12 h under high vacuum. A microporous physical adsorption analyzer (ASAP2020, Micrometrics Instruments, USA) for measuring N_2 adsorption and desorption isotherm of samples was also utilized to measure textural properties. UV–vis diffuse reflectance spectroscopy (DRS) was conducted on an Avantes AvaSpec 2048 TEC spectrophotometer. Thermogravimetric analysis (TGA) was performed on a Mettler Toledo TGA/DSC instrument in N_2 atmosphere at a 10 °C/min ramp rate 25–700 °C, using a sample mass of ~5 mg. Cyclic voltammetry (CV) experiments were conducted on a three electrode cell comprising of a glassy carbon working electrode, a Pt wire auxiliary electrode and a saturated Ag/AgCl reference electrode (Azar electrode Co, Urmia, Iran). PW12@PCN-222 suspension in acetone was drop-casted onto the polished glassy carbon electrode. The analysis of digested MOF samples for elemental contents was performed on an inductively coupled plasma optical emission spectroscopy (ICP-OES, Vista Pro). NMR spectra were recorded in CDCl_3 on a Bruker Avance 250 MHz NMR spectrometer operating at 250 MHz for ^1H NMR and 75 MHz for ^{13}C NMR. Electron paramagnetic resonance (EPR) spectra were recorded on a JEOL JES-FA2000 EPR spectrometer.

2.2. POM@PCN-222 preparation

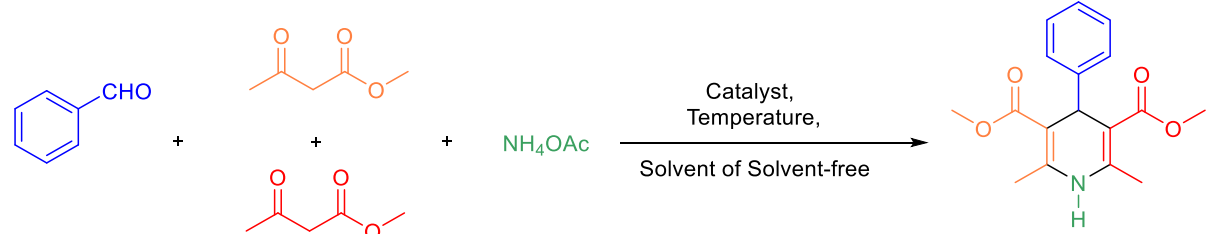
In a test tube, $\text{H}_3\text{PW}_{12}\text{O}_{40}$ (POM, $M_w=2880.17$ g/mol, 302 mg, 0.105 mmol) was added in 20 mL deionized water to a clear solution with pH ~2.5 was obtained. Free-base PCN-222 ($\text{C}_{96}\text{H}_{68}\text{N}_8\text{O}_{32}\text{Zr}_6$, $M_w\sim 2392.97$ g/mol, 45 mg, 0.018 mmol) was then transferred to the acidic solutions and rapidly sonicated. The suspension was then stirred occasionally at room temperature for 36 h. The resultant material was washed with water (three times) and acetone (three times) and dispersed in acetone for overnight followed by the acetone washing and drying under vacuum (2 h at 60 °C, and 4 h at 100 °C). The activated solid was submitted to the next set of experiments.

2.3. General method for the construction of 1,4-dihydropyridine derivatives

In a test tube, methyl acetoacetate (2 mmol), aromatic aldehyde (1 mmol), ammonium acetate (NH_4OAc , 1 mmol) and 10 mg of activated POM@PCN-222 (12 wt% of water was considered, equivalent to 0.0106 mmol of Zr(IV), 0.0035 mmol of TCPP, and 0.0016 mmol of POM as active sites considering the chemical formula $\text{Zr}_6(\mu_3\text{-OH})_4(\text{OH})_4(\text{H}_2\text{O})_4(\text{TCPP}=\text{C}_{48}\text{H}_{26}\text{N}_4\text{O}_8)_2(\text{H}_3\text{PW}_{12}\text{O}_{40})_{0.9}$, $M_w=4985.0$ g/mol) were added and magnetically stirred at 60 °C for the appropriate time (see Table 1). After end of the reaction as checked by TLC, the catalyst was isolated by adding ethylacetate (EtOAc). The solvent was evaporated and recrystallization in $\text{EtOH}/\text{H}_2\text{O}$ afforded the pure product. The characterization details and spectra (FT-IR, ^1H NMR, and ^{13}C NMR) are given in the Supplementary information.

Table 1

Optimization of the reaction conditions for the pseudo four-component Hantzsch 1,4-dihydropyridines synthesis.^a



Entry	Catalyst	Solvent or solvent-free	T (°C)	Time (h)	Yield (%) ^b	TON/TOF (h ⁻¹) ^c
1	-	Solvent-free	r.t.	24	-	-
2	POM@PCN-222 ^d	Solvent-free	r.t.	24	27	18/0.75
3	POM@PCN-222	Solvent-free	40	7.5	75	47.77/6.37
4	POM@PCN-222	Solvent-free	60	5	90	57.32/11.46
5	POM@PCN-222	Solvent-free	80	5	89	56.69/11.33
6	POM@PCN-222 ^e	Solvent-free	60	7	78	78/11.14
7	POM@PCN-222 ^f	Solvent-free	60	5	91	37.92/7.58
8	POM@PCN-222	EtOH	60	7	70	44.58/6.37
9	POM@PCN-222	EtOH	Reflux	7	77	49.04/7.01
10	POM@PCN-222	CH_3CN	60	10	70	44.58/4.46
11	POM@PCN-222	CH_3CN	Reflux	10	75	47.77/4.77
12	POM@PCN-222	$\text{CH}_3\text{CN}/\text{H}_2\text{O}$	Reflux	10	76	48.41/4.84
13	POM@PCN-222	H_2O	60	10	58	35.94/3.69
14	PCN-222	Solvent-free	60	8	60	38.22/4.78
15	TCPP	Solvent-free	60	5	16	10.19/2.04
16	$\text{ZrOCl}_2\cdot 8\text{H}_2\text{O}$	Solvent-free	60	5	47	29.94/5.99
17	POM	Solvent-free	60	5	71	45.22/9.04
18	PCN-222+POM ^g	Solvent-free	60	5	80	50.95/10.19

^a Reaction conditions: benzaldehyde (1 mmol), methyl acetoacetate (2 mmol), ammonium acetate (1 mmol), and catalyst (~1.6 mol%) under solvent or solvent-free conditions.

^b Yields refer to isolated and purified products.

^c TON (turnover number)=product (mmol)/catalyst (mmol), and TOF (turnover frequency)=TON/time (h).

^d POM@PCN-222 (10 mg, equivalent to 0.0106 mmol of Zr(IV), 0.0035 mmol of TCPP, and 0.0016 mmol of POM as active sites, total active sites=0.0157 mmol).

^e 1 mol%.

^f 2.4 mol%.

^g PCN-222 (1.41 mol%) and POM (0.16 mol%).

2.4. General method for visible-LED-light-driven photocatalytic synthesis of pyridine derivatives

In a test tube, methyl acetoacetate (2 mmol), aromatic aldehyde (1 mmol), ammonium acetate (NH_4OAc , 1 mmol), and 10 mg of POM@PCN-222 (equivalent to 0.0106 mmol of Zr(IV), 0.0035 mmol of TCPP, and 0.0016 mmol of POM as active sites considering the chemical formula $\text{Zr}_6(\mu_3\text{-O})_4(\mu_3\text{-OH})_4(\text{OH})_4(\text{H}_2\text{O})_4(\text{TCPP}=\text{C}_{48}\text{H}_{26}\text{N}_4\text{O}_8)_2(\text{H}_3\text{PW}_{12}\text{O}_{40})_{0.9}$, $M_w=4985.0$ g/mol) were added and magnetically stirred at 60 °C for the appropriate time (see Table 1). Acetonitrile (3–5 mL) was then added and the mixture was magnetically stirred and irradiated by visible-LED-light (a photoreactor system including 1 W LED lamps ($\sim 30,000$ lux, ~ 0.005 W/cm²)) and air conditioning/fans at room temperature under a molecular oxygen atmosphere (1 atm., balloon). After reaction completion as checked by TLC (n-hexane: EtOAc, 80:20, as eluent) (see Table 2), the photocatalyst was separated by centrifugation and washed with ethylacetate. The solvent was evaporated and recrystallization from EtOH/H₂O afforded the pure product (the product was also purified using flash chromatography; EtOAc /petroleum ether). The characterization details and spectra (FT-IR, ¹H NMR, and ¹³C NMR) are given in the Supplementary information.

3. Results and discussion

3.1. POM@PCN-222 characterization

PCN-222 consisting of TCPP linkers and $\text{Zr}_6(\mu_3\text{-O})_4(\mu_3\text{-OH})_4(\text{OH})_4(\text{H}_2\text{O})_4$ nodes (Zr_6 nodes) was obtained using a slight modification from the literature protocol and then characterized [40]. POM-functionalized PCN-222, denoted here POM@PCN-222, was subsequently synthesized according to an impregnation method as described in the experimental section. An effective and facile technique to incorporate POMs into a 3D MOF is impregnation and requires large pore sizes (>10 Å) in the MOF for POM diffusion [19,23].

ICP-OES analysis based on the amount of zirconium and tungsten showed a POM, $\text{H}_3\text{PW}_{12}\text{O}_{40}$, loading in PCN-222 ca. 0.9 POM per Zr_6 -node with 9.90 wt% of Zr and 35.90 wt% of W contents, representing, to date, a remarkable POM loading in a POM@MOF material (Table S1) [14,19].

Particle size and surface morphology of PCN-222 and POM@PCN-222 were also analyzed using SEM and TEM. SEM images display hexagonal rod-like crystals with a length of ~ 1 to 2.5 μm and width of 80–250 nm, with no change in shape and dimension of primary PCN-222 particles observed upon POM incorporation (Fig. 1, Fig. S1). No POM accumulation or aggregation on the MOF could be visualized (Fig. S1).

Energy dispersive X-ray spectroscopy (EDX) analyses of PCN-222 and POM@PCN-222 were performed as shown in Figs. S2 and S3. EDX analysis of POM@PCN-222 confirmed POM incorporation into PCN-222 and the successful synthesis of POM@PCN-222 with the presence of phosphorus (0.01 at%) and tungsten (2.78 at%) elements as compared to the elemental pattern of PCN-222. In addition, EDX elemental mapping in Fig. 2 clearly revealed a homogeneous distribution and dispersion of C, N, O, W, P, and Zr through the composite, confirming that POMs are predominantly located within PCN-222 pores.

HRTEM images of POM@PCN-222 further depicted (and confirmed) the uniform distribution with no agglomerates of POM particles over the MOF (Fig. 3).

Measured powder X-ray diffraction (PXRD) pattern of POM@PCN-222 exhibited peaks indicative of the PCN-222 structure, regarding patterns of as-synthesized MOF as well as that simulated from single crystal data (Fig. 4) [41], with characteristic diffraction peaks at 2θ of

2.5°, 4.8°, 6.6°, 7.1°, 8.3°, 9.7° and 9.9°, respectively, corresponding to (100), (200), (2-11), (201), (3-11), (400) and (4-21) crystal planes. With POMs immobilized within PCN-222, signals were only slightly less intense as compared to those of the pristine MOF. These changes resulted from the incorporation of POMs within the MOF's meso-channels. Moreover, PXRD patterns of POM@PCN-222 did not show any POM diffraction peaks, indicating most probably an optimum dispersion of POM within MOF's pores.

The resulting Brunauer-Emmett-Teller (BET) surface area from the nitrogen isotherm dramatically decreased from unfunctionalized PCN-222 (~ 2000 m²/g) to POM@PCN-222 (~ 770 m²/g), in any case with high surface area values (Fig. 5, top). The observed decline in surface area after modification is due to POM loading within the pores, whereas accessible high porosity is still maintained. POM@PCN-222 was shown to be mesoporous with a steep increase at around $P/P_0=0.3$, similar to that of PCN-222, via characteristic type IV nitrogen adsorption-desorption curves according to the IUPAC classification. This indicated that the framework structure of the pristine PCN-222 support with eight-coordinated Zr(IV) nodes to TCPP linkers remained intact upon direct impregnation for POM incorporation. Pore size distributions (PSDs), calculated from the DFT model using desorption isotherms at -196 °C, disclose a significant reduction mainly in the large hexagonal pores from 30 Å to 25 Å, associated to a partial pore filling (small channels) after POM incorporation into PCN-222 (Fig. 5, bottom). These results pointed again to POMs located within MOF's pores. Such pore sizes in POM@PCN-222 are still large enough for an efficient diffusion of guest molecules and reactant-accessible catalytically active sites. All results combined confirmed the successful synthesis of both PCN-222, in accordance to previous work [40,41], and POM@PCN-222.

Thermal gravimetric analysis (TGA) for the samples under N₂ atmosphere from ambient temperature to 700 °C revealed approximately 39% of weight loss for POM@PCN-222 as compared to that of activated PCN-222 (weight loss $\sim 31\%$) (Figs. S4 and S5). Comparatively, there was a major weight loss profile at around 100 °C, as further evidenced by differential scanning calorimetry (DSC), due to the evolution of water molecules of the POM, H-bonded to Zr_6 clusters of PCN-222. This measurement pointed out that POM@PCN-222 is hygroscopic and tends to adsorb water (almost 12% of the material weight). The next step of decomposition over a temperature range of ~ 350 to 550 °C is due to the degradation of TCPP organic linkers.

UV-Vis diffuse reflectance spectroscopy (DRS) of POM@PCN-222 showed more intense charge transfer bands, mainly around 400 and 700 nm, as compared to those of PCN-222 (Fig. 6), further confirming POM immobilization. The enhanced response of the composite in the visible light domain can favor photocatalytic applications. Optical HOMO-LUMO gap (E_g) value for the POM@PCN-222 was calculated ~ 1.57 eV from UV-Vis-DRS using the Tauc plot method by the intercept of the tangent to the plot of $(\alpha h\nu)^{1/2}$ versus the photon energy ($h\nu$) (Fig. S6) [45,46].

To further assess the structure integrity and the redox behavior of the composite POM@PCN-222, cyclic voltammetry (CV) was employed. As the results shown (Figs. S7 and S8), the redox capability of POM in PCN-222 was predominantly maintained, although a minor change in reduction potentials as compared to the pristine POM is observed. This supported the existence of a relevant interaction between the POM and PCN-222 [23,47].

The successful incorporation of the POM into PCN-222 could also be confirmed by Fourier transform infrared (FT-IR) spectroscopy. FTIR spectra of POM@PCN-222 showed the appearance of the new peaks at 810, 892, 986, and 1080 cm⁻¹ as compared to untreated PCN-222, which can be correlated, respectively, to W-O-W, W-O_{cubic}-W, W=O and P-O stretching bands of POM (Figs. S9) [48].

Table 2POM@PCN-222 catalyzed synthesis of 1,4-dihydropyridines.^a

X = H, 4-NO ₂ , 3-NO ₂ , 4-Cl, 4-OMe				
Entry	Product	Time (h)/Isolated yield (%)	TON/TOF (h ⁻¹) ^b	M.p. (°C) [lit.] ^{ref}
1		5/90	57.32/11.46	199–200 °C [197–199 °C] ³²
2		6.5/88	56.05/8.62	169–170 °C [167–169 °C] ²⁹
3		7/90	57.32/8.19	211–212 °C [210–212 °C] ²⁹
4		8/89	56.69/7.08	196–198 °C [197–199 °C] ²⁹
5		7.5/88	56.05/7.5	185–187 °C [186–188 °C] ²⁹

^a Reaction conditions: aromatic aldehyde (1 mmol), methyl acetoacetate (2 mmol), ammonium acetate (1 mmol), and POM@PCN-222 (10 mg, equivalent to 0.0106 mmol of Zr(IV), 0.0035 mmol of TCP, and 0.0016 mmol of POM as active sites, total active sites=0.0157 mmol, ~1.6 mol%) under solvent-free conditions at 60 °C.

^b TON (turnover number)=product (mmol)/catalyst (mmol), and TOF (turnover frequency)=TON/time (h).

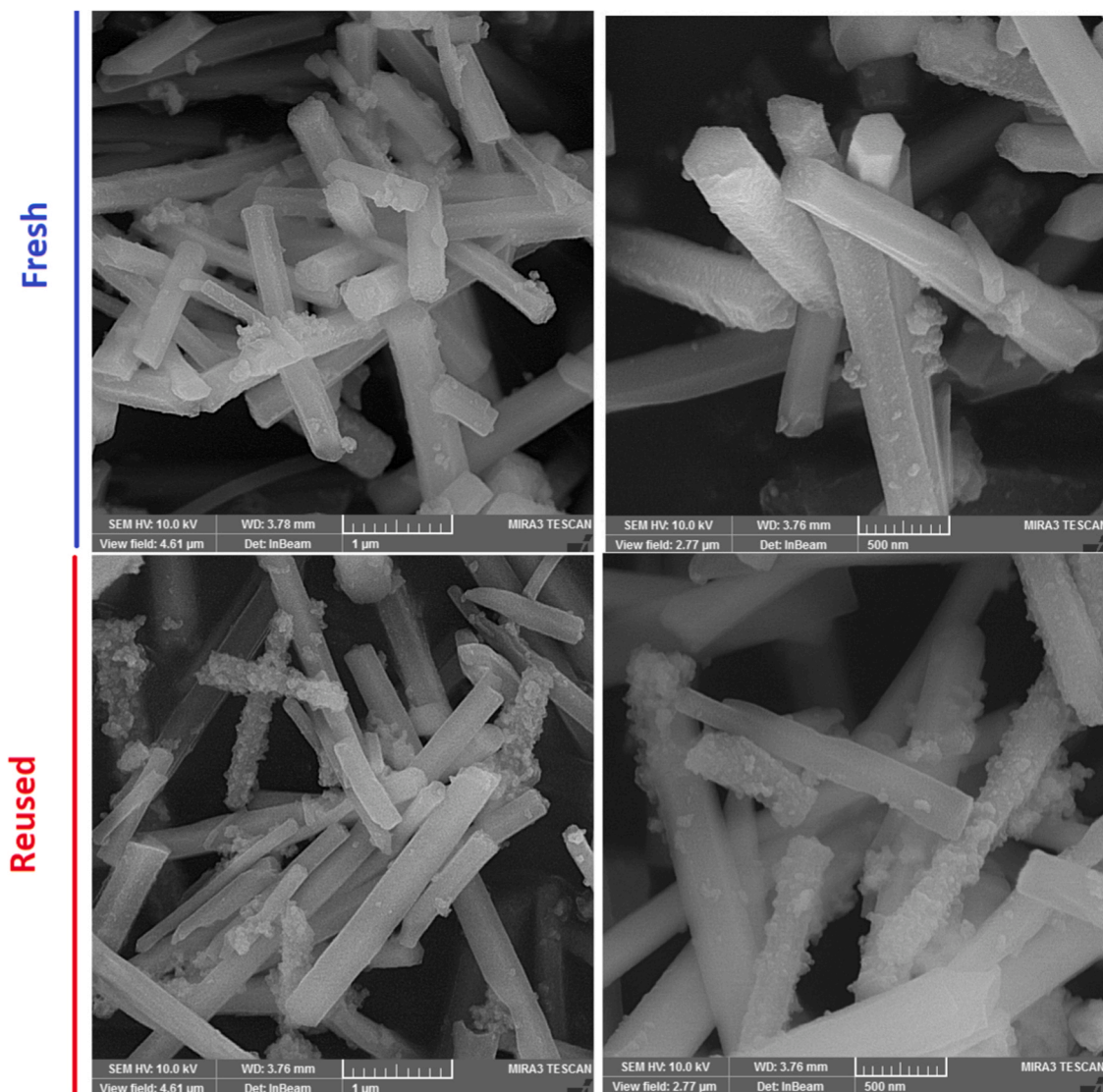


Fig. 1. Scanning Electron Microscopy (SEM) images of: (a) fresh POM@PCN-222, (b) reused POM@PCN-222. The scale bars are 1 μm and 500 nm.

3.2. Photocatalytic activity of POM@PCN-222

After synthesis and characterization of POM@PCN-222, the composite was employed as a new multifunctional catalyst for the multi-component syntheses of 1,4-dihydropyridines and pyridine derivatives. With this purpose, the *pseudo* four-component reaction of benzaldehyde, methyl acetoacetate, and ammonium acetate in molar ratio 1:2:1 was selected as a model reaction. We firstly attempted to optimize the synthesis of the 1,4-dihydropyridine, as intermediate during pyridine synthesis [38] utilizing POM@PCN-222. Different reaction conditions for the synthesis of 1,4-dihydropyridines using the representative model are summarized in Table 1.

The model reaction did not proceed in the absence of catalyst and solvent (Table 1, entry 1), while proceeded using the POM@PCN-222 catalyst (10 mg, ~ 1.6 mol%) at room temperature under solvent-free conditions (Table 1, entry 2). Next, the reaction was screened at various temperatures and solvent-free conditions by using POM@PCN-222 (Table 1, entries 2–5). An increase in temperature from ambient to 60 $^{\circ}\text{C}$ led to increased product yields at shorter reaction time and turnover frequency (TOF) from 0.75 h^{-1} to 11.46 h^{-1} (Table 1, entries 2–4). Further increasing the temperature to 80 $^{\circ}\text{C}$ did not influence the reaction yield (Table 1, entry 5). The effect of POM@PCN-222 amount on reaction time and product yield of the product was then evaluated

under solvent-free conditions at 60 $^{\circ}\text{C}$ (Table 1, entries 5–7). When the catalyst amount was decreased, the decreased product yield (from 90% to 78%) was associated to an increase in reaction time from 5 h to 7 h and a decrease in TOF from 11.46 h^{-1} to 11.14 h^{-1} (Table 1, entry 4 versus entry 6). An additional increase in catalyst loading was not worthwhile (Table 1, entry 4 versus entry 7), thereby, avoiding the excess consumption of the catalyst (10 mg of POM@MOF was chosen as the optimum). To further adjust the conditions, the role of the solvent (EtOH, H_2O , CH_3CN , and $\text{CH}_3\text{CN}/\text{H}_2\text{O}$) and solvent-free conditions were also considered in the reaction (Table 1, entries 4 and 8–13). Among all evaluated conditions, solvent-free conditions delivered the highest yield of 90% at shortest reaction times with TON of 57.32 and TOF of 11.46 h^{-1} (Table 1, entry 4). Under identical conditions, unfunctionalized PCN-222 provided only 60% of product yield after a prolonged reaction time of 8 h with TOF of 4.78 h^{-1} (Table 1, entry 14) as compared to POM@PCN-222 (TOF=11.46 h^{-1}). This catalytic activity of PCN-222 could be due to the existence of Lewis acidic Zr_6 -node sites and basic sites of porphyrin linkers of PCN-222 [41,49,50]. Furthermore, control tests with TCPP and $\text{ZrOCl}_2 \cdot 8\text{H}_2\text{O}$, respectively, as MOF linker and Zr-node precursor obviously confirmed their active roles in the catalytic process (Table 1, entries 15 and 16). However, yields and TOF were significantly reduced as compared to those observed for POM@PCN-222. When pristine POM was used as catalyst under

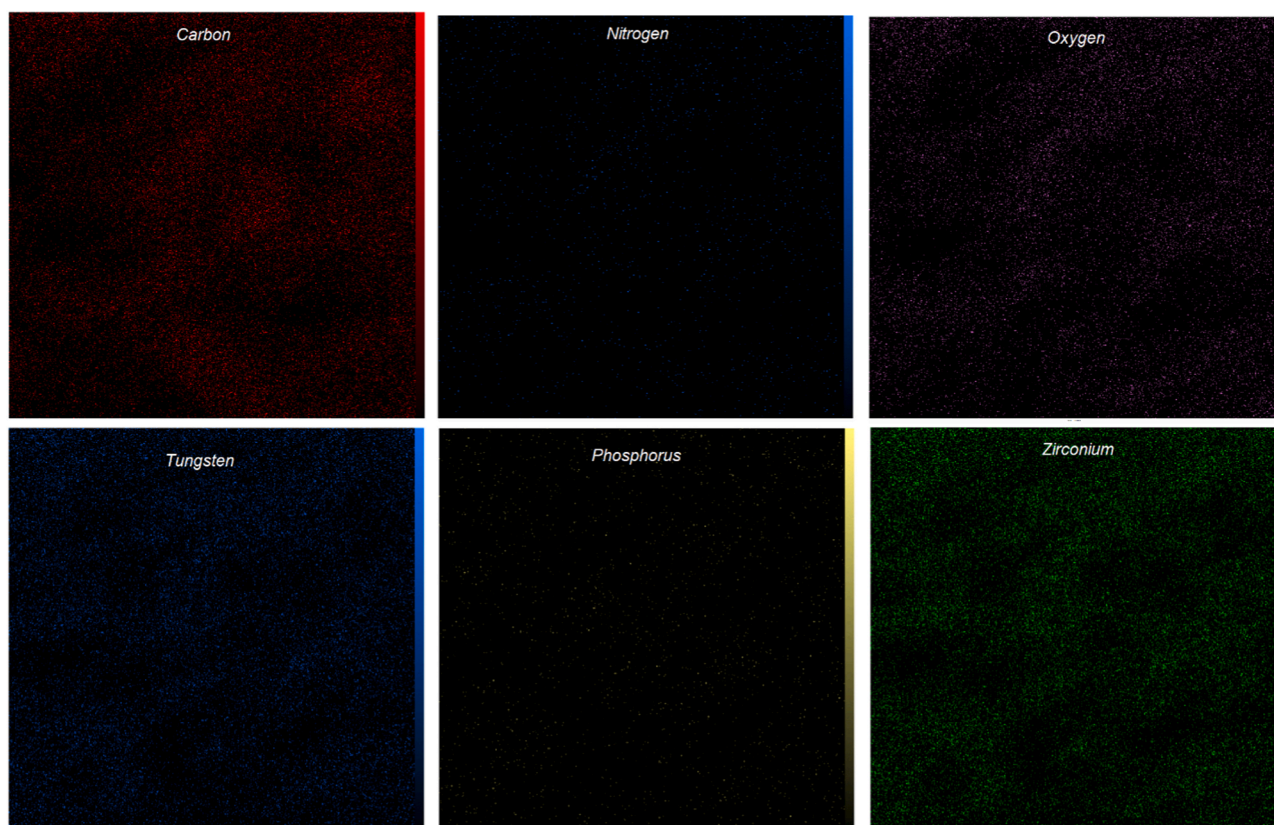


Fig. 2. EDX elemental mapping of POM@PCN-222.

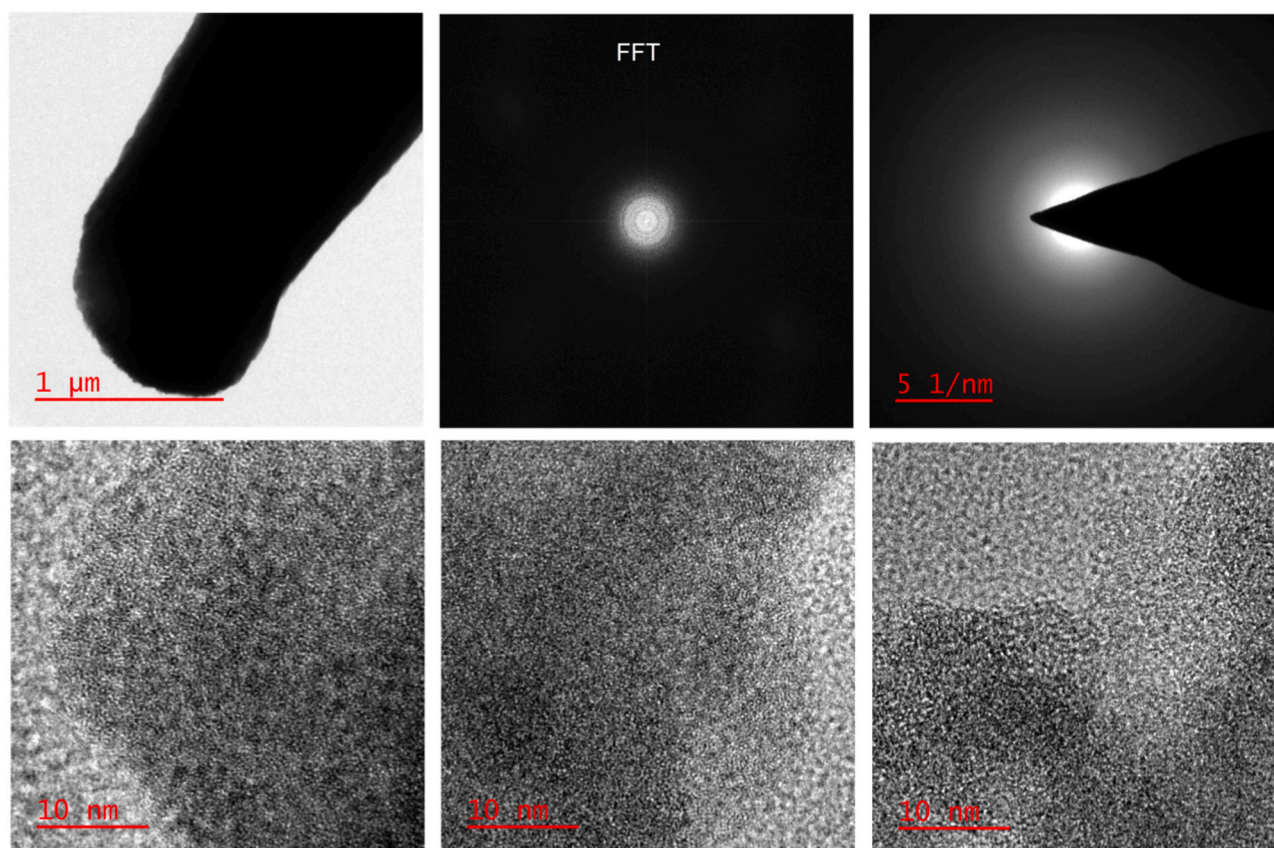


Fig. 3. HRTEM images of POM@PCN-222.

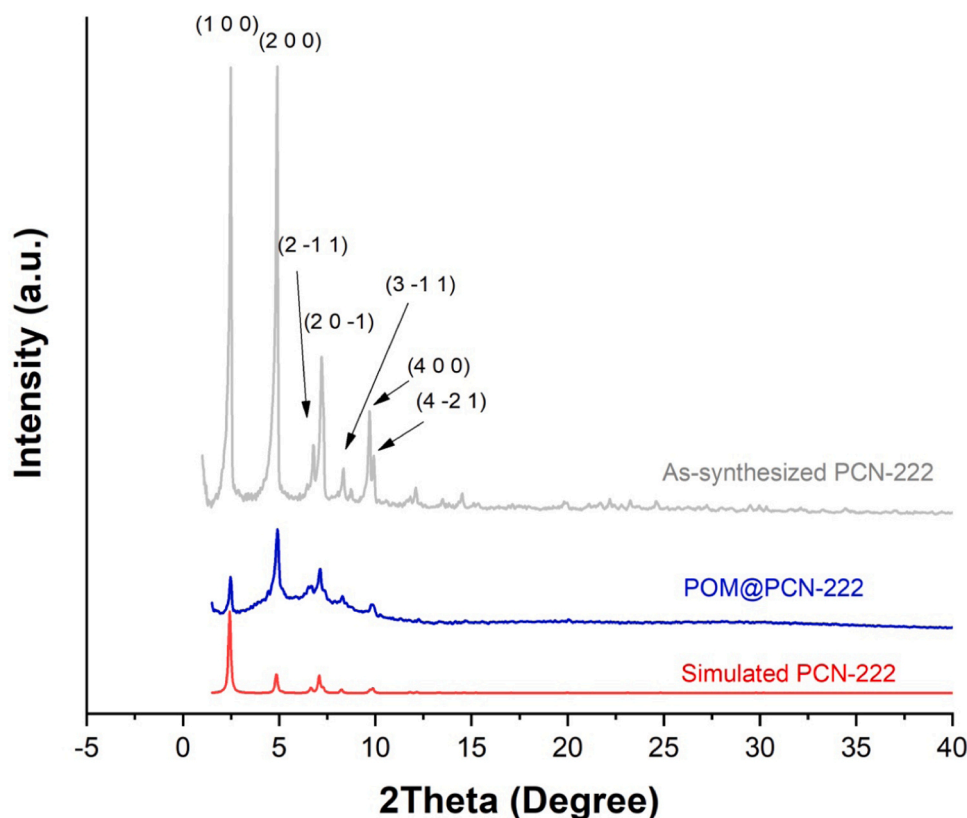


Fig. 4. PXRD patterns of simulated PCN-222, as-synthesized PCN-222 and POM@PCN-222.

optimized conditions, the reaction was effectively promoted; with 71% product yield after 5 h (TOF 9.04 h^{-1} , entry 17).

To further study the role of the active sites and the support, PCN-222 (equimolar in Zr and TCPP in POM@PCN-222) was physically mixed with POM (equimolar in POM to POM@PCN-222) and tested as catalyst for the reaction (entry 18). Product yield was 80% (TOF $=10.19 \text{ h}^{-1}$) which is comparatively lower to that using POM@PCN-222 as catalyst (Yield=90% and TOF $=11.46 \text{ h}^{-1}$). These results point out that Zr clusters, TCPP linkers, and POM (mainly) in POM@PCN-222 act as catalytically active sites in the reaction. In addition, the superior activity of POM@PCN-222 could be due to the site-isolation of PW_{12} active sites within the MOF, synergetic effect between MOF and POM, and preferred accessible active sites achieved by employing 3D hierarchically ordered porous structure of the MOF as a support.

Considering the interesting results from the optimized conditions by using the hybrid material, to investigate the generality of this protocol, the various aromatic aldehydes were then explored and afforded a series of 1,4-dihydropyridines (Table 2) in reasonable yields, presenting TONs reaching from 56.05 to 57.32 (TOFs $=7.08\text{--}11.46 \text{ h}^{-1}$).

Innovatively, motivated by the oxidation of 1,4-DHPs as calcium channel blockers to the corresponding pyridine derivatives by using cytochrome P-450 in liver [31], the feasibility of the use of POM@PCN-222 as bio-mimetic catalyst for the preparation of pyridines was subsequently explored (Table 3).

Excitingly, the solvent-free reaction between aromatic aldehydes, methyl acetoacetate, and ammonium acetate led to formation of 1,4-dihydropyridines in the presence of POM@PCN-222 (10 mg) (Table 2). The further visible-light-induced oxidation of 1,4-dihydropyridines to the corresponding pyridines (without further purification) was further investigated (Tables S2 and 3). Control tests are given in Table S2 and showed that light source, acetonitrile as solvent and POM@PCN-222 as photocatalyst are all vital for the LED photocatalytic step. As shown in Table S2, the reaction does not proceed when the catalyst is not

present or when $\text{ZrOCl}_2 \cdot 8\text{H}_2\text{O}$ as Zr-node precursor or UiO-66 involving of Zr-oxo cluster and terephthalic acid were employed (entries 1–5 in Table S2). In contrast, 1,4-dihydropyridine was efficiently formed and subsequently converted to the corresponding pyridine within 28 h in CH_3CN when POM@PCN-222 was employed as catalyst (entries 6–8). Using pristine PCN-222 and POM as catalyst, the photooxidation process was also promoted; with however reduced yields as compared to the use of POM@PCN-222 (entries 9 and 10). These experiments pointed out that TCPP and POM groups in POM@PCN-222 act as photocatalytically active centers in the photooxidation process. It should be noted that the production reaction of pyridines promoted by PCN-222 was found to be faster with respect to that of TCPP (entries 10 and 11). This observation is ascribed to the avoidance of the well-known self-aggregation/destruction of TCPP linkers due to connection with Zr-oxo nodes to build up the MOF material.

Interestingly, all reactions proceeded smoothly and afforded excellent yields with different aromatic aldehydes and TONs ranging from 43.31 to 47.77 (Table 3). The catalytic efficiency of POM@PCN-222 is even more remarkable when one reflects that the actual number of active catalytic sites is only a part of the introduced $\sim 1.6 \text{ mol\%}$ loading. *In-situ* formed 1,4-dihydropyridines through solvent-free conditions and their straight use for the oxidation under visible LED light illumination is noticeably smooth and clean.

The reusability of POM@PCN-222 for the one-pot visible-light driven synthesis of dimethyl 2,6-dimethyl-4-phenylpyridine-3,5-dicarboxylate was subsequently attempted by removing the catalyst, washing it with ethyl acetate and drying under vacuum. The recovered POM@PCN-222 was then reused for next run which showed a slight decrease in product yield from 72% to 62% after three consecutive runs, as given in Table 3. The recovered catalyst was also examined by FT-IR, SEM, EDX elemental mapping, PXRD, and ICP-OES. SEM images of the reused catalyst indicate nearly identical morphology after the third run (Fig. 1). In addition, the FT-IR of the fresh sample and the recycled are approximately

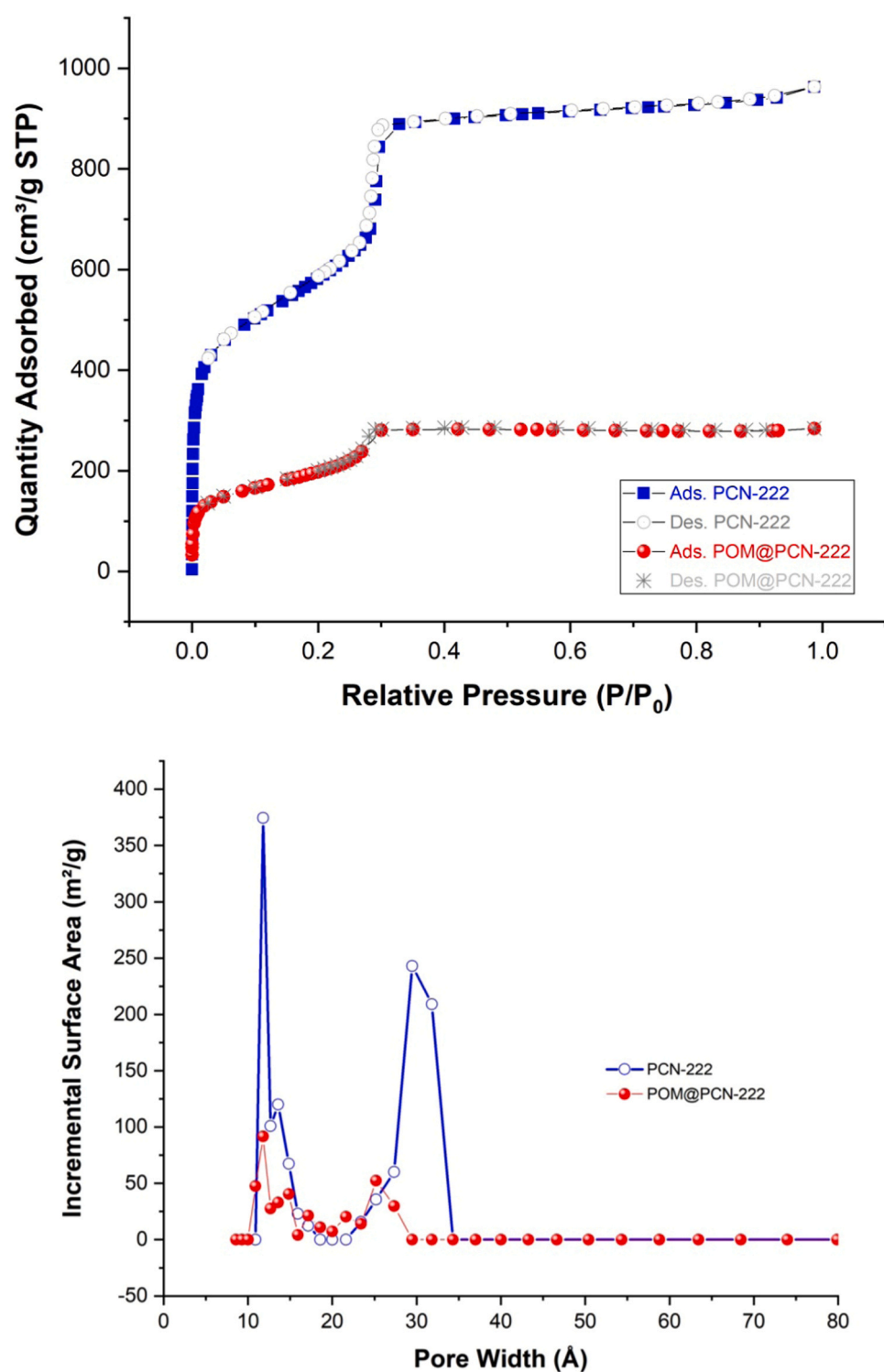


Fig. 5. N_2 adsorption isotherms of PCN-222 and POM@PCN-222 at 77 K (top) and DFT-calculated pore size distributions of PCN-222 and POM@PCN-222 (bottom).

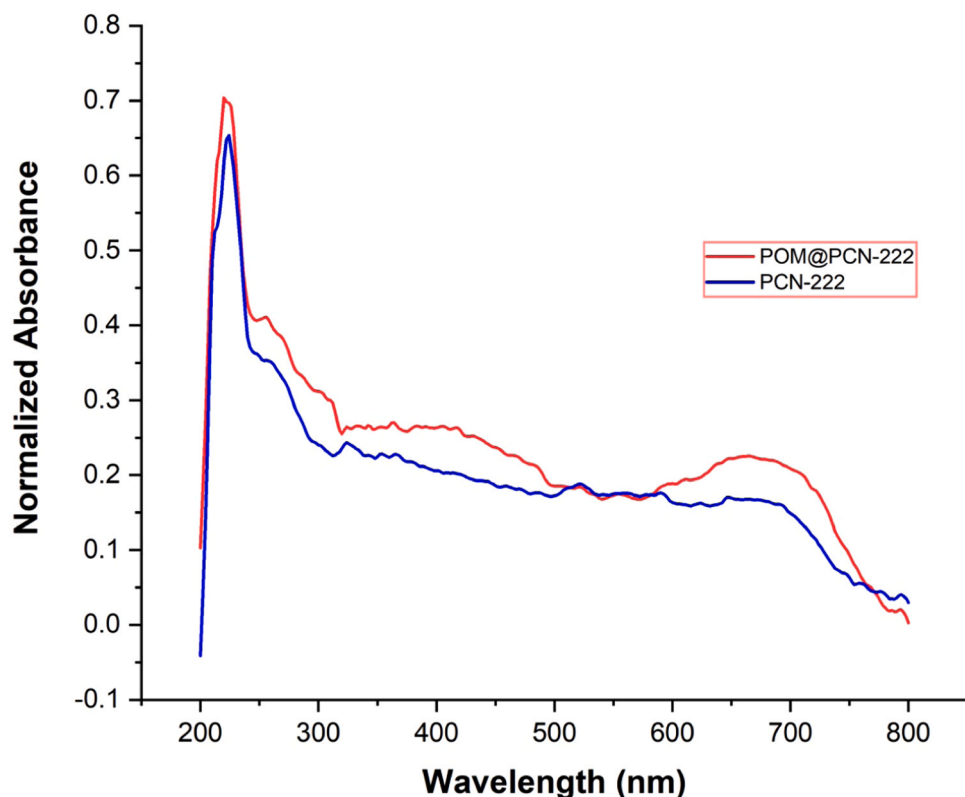


Fig. 6. UV-Vis diffuse reflectance spectra (DRS) of a) PCN-222 and b) POM@PCN-222.

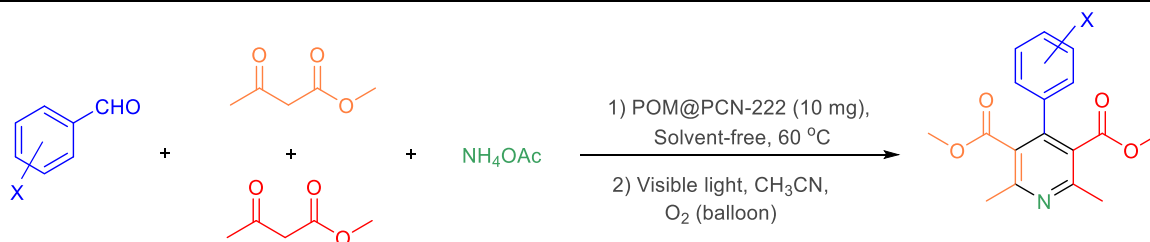
identical (Figs. S9). ICP-OES analysis of the reused POM@PCN-222 showed ~ 0.8 POM per Zr_6 -node and only a small amount of POM (~ 2 wt%) leaching during the process (Table S2). PXRD analysis of the reused catalyst confirmed that the crystallinity of POM@PCN-222 was retained over the reusing test (Fig. S10). EDX mapping of the reused catalyst (Fig. S11 vs Fig. 2) showing that tungsten and phosphorus are homogeneously dispersed throughout the MOF support (same as that of the fresh one). Furthermore, the stability of POM@PCN-222 was investigated by filtering off the catalysts after 10 h of reaction time (product yield ca. 42%) after which the reaction process was further followed in the absence of catalyst. The reaction did not further progress, with product yields obtained only increasing to 46% after 28 h (Table S2). These results strongly confirm the heterogeneous nature of the reaction catalyzed by POM@PCN-222 with small quantities of POM leaching during the reaction. All data confirmed POM@PCN-222 as stable and reusable multifunctional (photo)catalyst.

These results together confirmed that the combination of the PW_{12} , having strong Lewis and redox acid sites, with PCN-222 did not only showed superior activity with respect to the individual components (Table 1 and Table S2), but can also circumvent major limitations owing to POMs including handling problem, low surface area and high solubility in solution (making problematic its reuse [13]). The porphyrin-based framework, PCN-222, as highly porous and light-sensitive support plays a vital role since it assists electron transfers, increases the surface area and stabilizes the POM species. The strong POM interaction with PCN-222 is due to hydrogen bonding between Zr-OH nodes and the oxo-groups of the POM, displacement of hydroxyl ions with $[PW_{12}O_{40}]^{3-}$ on Zr_6 nodes, acid-base interaction between free-base porphyrin of PCN-222 and the acidic sites of the POM and van der Waals interactions between both structures [19,23].

To gain insights into the reaction mechanism of one-pot pyridines synthesis from methyl acetoacetate, aromatic aldehydes and ammonium acetate catalyzed by POM@PCN-222, product formation was monitored by FT-IR spectroscopy at different time intervals (Figs. S12 and S13).

Spectra clearly confirmed the production pathways of pyridine through photooxidation of *in-situ* formed 1,4-dihydropyridine intermediate. As shown in Fig. S12, when the reaction time was increased from 30 min to 300 min, N-H and C=O stretching vibrations, respectively, at 3344 and 1699 cm^{-1} , related to 1,4-dihydropyridine's structure were apparently intensified, along with consumption of the starting materials. This proves the first catalytic step and cyclization and condensation reactions between starting materials towards formation of key 1,4-dihydropyridine intermediates. After that, in the presence of oxygen (1 atm.), CH_3CN and visible-LED-light irradiation, the reaction was further continued. As reaction time goes on, steady formation of pyridine was confirmed by FT-IR spectra monitoring (Fig. S13) with gradual disappearance of N-H band of 1,4-dihydropyridine at 3344 cm^{-1} . Additionally, a nominal C=O band shift from 1699 cm^{-1} to 1730 cm^{-1} (the characteristic absorption band of pyridine) is progressively detected (Fig. S13) along with pyridine formation. This demonstrated dehydrogenation/aromatization of 1,4-dihydropyridine towards formation of the final product. During FT-IR monitoring, peak intensities were dynamically changed on the road to the final product formation during the reaction, representing the high accessible catalytic sites of POM@PCN-222 for the reactants.

The mechanism for the preparation of pyridines using POM@PCN-222 both as a catalyst and photocatalyst has been depicted in Scheme 2, as supported by experiments mentioned above and reported in literature [22,38,46,51,52]. At the beginning, POM@PCN-222, having porphyrin photosensitizer groups [52] and Lewis acids [6,14], activate the aldehyde for the nucleophilic addition of enol form of methyl acetoacetate (1) to provide the related Knoevenagel intermediate (2). *In situ* formed ammonia from ammonium acetate subsequently attacks the second methyl acetoacetate activated by the catalyst to give the enamine intermediate (3). The formed enamine (3) can then react with the activated Knoevenagel intermediate (2) via Michael addition to afford intermediate (4). In the next stages, cyclization and condensation reactions take place and the dihydropyridine (5) is formed. Upon visible

Table 3Visible-light promoted one-pot two-step synthesis of pyridine derivatives.^aX = H, 4- NO_2 , 3- NO_2 , 4-Cl, 4-OMe

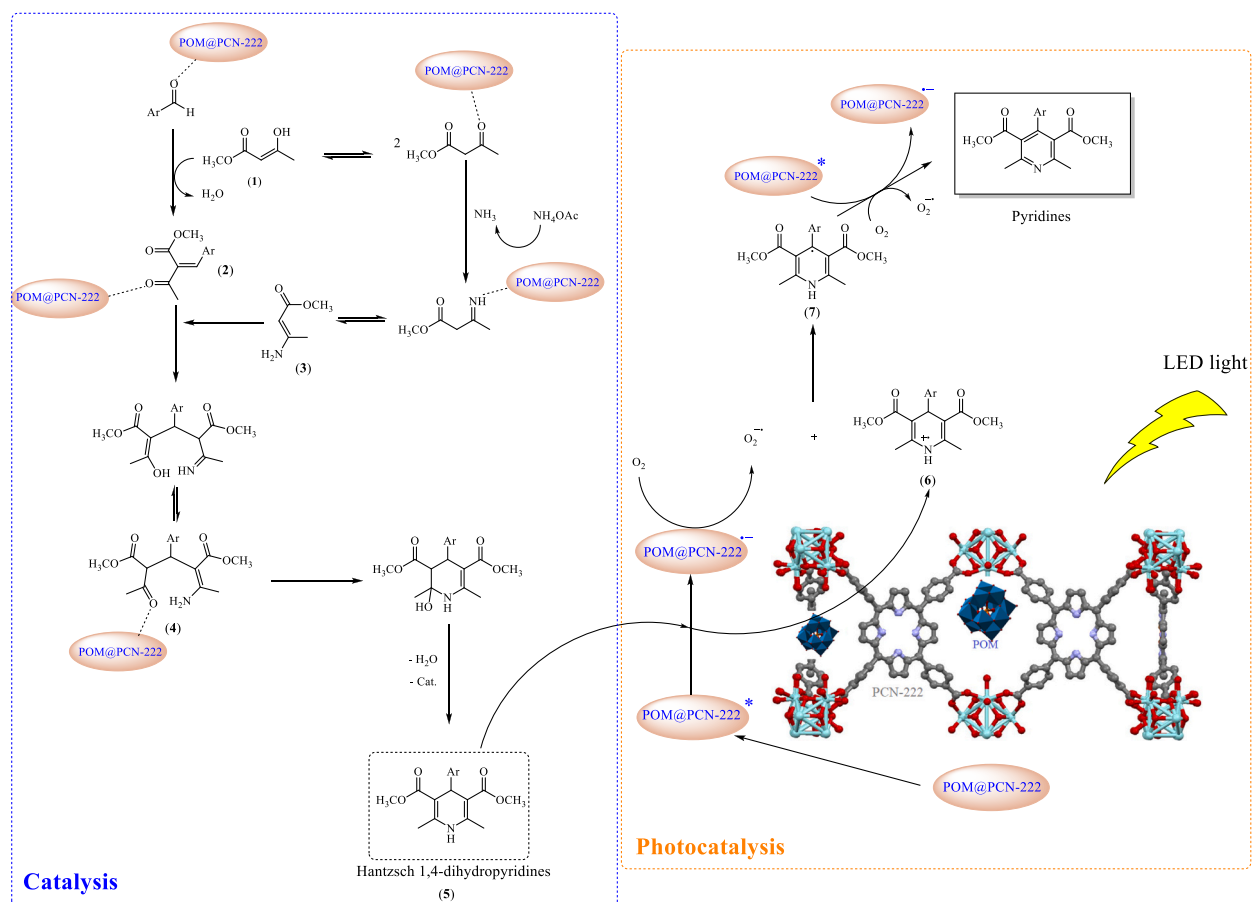
TON/TOF (h^{-1}) ^b	Isolated yield (%)	Time (h)			Product	Entry
		Overall	Step 2 (photocatalysis)	Step 1 (catalysis)		
45.86/1.4	72, 64, ^c 62 ^d	33	28	5		1
38.21/1.25	60	30.5	24	6.5		2
44.59/1.14	70	39	32	7		3
47.77/1.19	75	40	32	8		4
43.31/1.11	68	39	32	7		5

^a Reaction conditions: aromatic aldehyde (1 mmol), methyl acetoacetate (2 mmol), ammonium acetate (1 mmol), POM@PCN-222 (10 mg, equivalent to 0.0106 mmol of Zr(IV), 0.0035 mmol of TCPP, and 0.0016 mmol of POM as active sites, total active sites=0.0157 mmol) under solvent-free condition at 60 °C, (*first step*), without purification, just followed by addition of CH_3CN (3 mL), O_2 (1 atm.), and visible LED light irradiation, (*second step*).

^b TON (turnover number)=product (mmol)/catalyst (mmol), and TOF (turnover frequency)=TON/time (h).

^c Reusability of the catalyst in 2th cycle.

^d Reusability of the catalyst in 3th cycle.



Scheme 2. Proposed mechanism for visible light driven one-pot synthesis of pyridines using multifunctional POM@PCN-222.

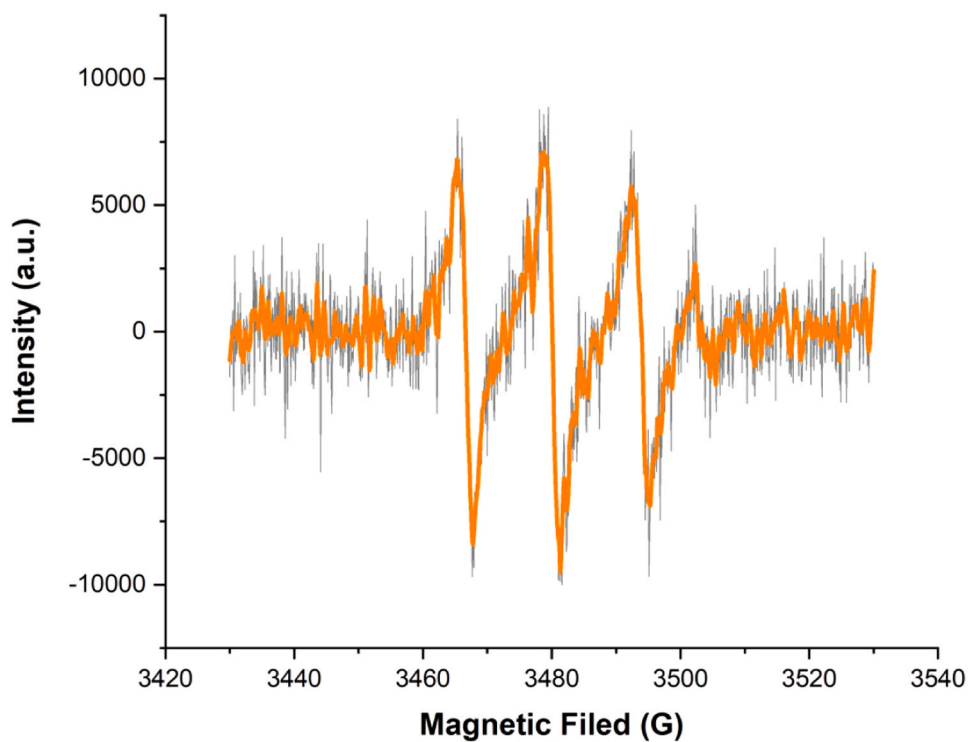


Fig. 7. EPR measurement of superoxide ($\text{O}_2^{\bullet-}$) species generated by POM@PCN-222.

light irradiation on POM@PCN-222 photocatalyst, the excited species POM@PCN-222* is formed and reductively quenched by the dihydropyridine (5) via a single electron transfer (SET) to give a radical cation (6) and radical anion POM@PCN-222^{•−}. Next, the radical anion POM@PCN-222^{•−} transfers an electron to O₂, generating superoxide radical anions O₂^{•−} and regenerating POM@PCN-222. The proton abstraction from (6) by active oxygen species O₂^{•−} generates intermediate (7), which loses one electron to afford the pyridine as desired product.

To provide deep insights into the reaction mechanism, EPR experiments were additionally conducted at room temperature on O₂^{•−} captured by 5,5-dimethyl-1-pyrroline N-Oxide (DMPO) as a superoxide radical trapping agent, to confirm the presence of *in-situ* generated superoxide species (O₂^{•−}). After visible light irradiation, characteristic EPR signals of the superoxide radical were detected as comparatively not observed in the dark, evidently proving the formation of O₂^{•−} as reactive oxygen species in the reaction (Fig. 7).

4. Conclusions

A porphyrinic Zr-MOF with photothermal properties, PCN-222, was prepared via assembly of a porphyrin-based ligand and zirconium chloride utilizing TFA and BA as modulators, followed by post-modification with a POM, H₃PW₁₂O₄₀, to render a novel porous POM@PCN-222. This system was found to have an excellent photocatalytic activity in the efficient synthesis of pyridines, affording 1,4-dihydropyridines intermediates *in-situ* from *pseudo* four-component reaction between aldehydes, methyl acetoacetate, and ammonium acetate, followed by their photo-oxidation under visible LED illumination in the presence of O₂ as green oxidant. An increased catalytic performance was observed for the composite as compared to the pristine materials, due to synergistic effect between the MOF and the POM. Interestingly, the strong interaction between PCN-222 and POM prevented POM leaching during the reaction and the composite was highly active up to three reaction runs. The reaction mechanism was suggested, using control tests, EPR and FT-IR reaction monitoring. Based on our knowledge, this is first example of synthesis of pyridines from aldehydes without using any additive and is fundamentally important reaction type for both pharmaceuticals preparation and organic synthesis. We believe this work illustrates the potential of MOFs as attractive supports for the design and development of advanced functional heterogeneous (photo)catalysts for selective synthetic organic reactions.

Declaration of Competing Interest

The authors declare that they have no known competing financial interests or personal relationships that could have appeared to influence the work reported in this paper.

Acknowledgments

This work was supported by the University of Zabol (Grant numbers: IR-UOZ-GR-9381). This paper has been supported by the RUDN University Strategic Academic Leadership Program (R. Luque).

Appendix A. Supporting information

Supplementary data associated with this article can be found in the online version at doi:10.1016/j.apcatb.2021.120815.

References

- [1] J. Qiu, X. Zhang, Y. Feng, X. Zhang, H. Wang, J. Yao, Modified metal-organic frameworks as photocatalysts, *Appl. Catal. B* 231 (2018) 317–342.
- [2] H. Li, F. Zhai, D. Gui, X. Wang, C. Wu, D. Zhang, X. Dai, H. Deng, X. Su, J. Diwu, Z. Lin, Z. Chai, S. Wang, Powerful uranium extraction strategy with combined

- ligand complexation and photocatalytic reduction by postsynthetically modified photoactive metal-organic frameworks, *Appl. Catal. B* 254 (2019) 47–54.
- [3] A. Melillo, M. Cabrero-Antonino, S. Navalón, M. Alvaro, B. Ferrer, H. García, Enhancing visible-light photocatalytic activity for overall water splitting in UiO-66 by controlling metal node composition, *Appl. Catal. B* 278 (2020), 119345.
- [4] X. Zhang, M.C. Wasson, M. Shayan, E.K. Berdichevsky, J. Ricardo-Noordberg, Z. Singh, E.K. Papazyan, A.J. Castro, P. Marino, Z. Ajoyan, Z. Chen, T. Islamoglu, A. J. Howarth, Y. Liu, M.B. Majewski, M.J. Katz, J.E. Mondloch, O.K. Farha, A historical perspective on porphyrin-based metal-organic frameworks and their applications, *Coord. Chem. Rev.* 429 (2021), 213615.
- [5] F. Li, Y. Tian, S. Su, C. Wang, D.-S. Li, D. Cai, S. Zhang, Theoretical and experimental exploration of tri-metallic organic frameworks (t-MOFs) for efficient electrocatalytic oxygen evolution reaction, *Appl. Catal. B* 299 (2021), 120665.
- [6] K. Epp, A.L. Semrau, M. Cokoja, R.A. Fischer, Dual site lewis-acid metal-organic framework catalysts for CO₂ fixation: counteracting effects of node connectivity, defects and linker metalation, *ChemCatChem* 10 (2018) 3506–3512.
- [7] A. Kirchon, L. Feng, H.F. Drake, E.A. Joseph, H.-C. Zhou, From fundamentals to applications: a toolbox for robust and multifunctional MOF materials, *Chem. Soc. Rev.* 47 (2018) 8611–8638.
- [8] J.-D. Xiao, H.-L. Jiang, Metal-organic frameworks for photocatalysis and photothermal catalysis, *Acc. Chem. Res.* 52 (2019) 356–366.
- [9] M. Hao, Z. Li, Visible light-initiated synergistic/cascade reactions over metal-organic frameworks, *Sol. RRL* 5 (2021), 2000454.
- [10] M. Hao, Z. Li, 21 – light-induced organic transformations over some MOF materials, in: X. Wang, M. Anpo, X. Fu (Eds.), *Current Developments in Photocatalysis and Photocatalytic Materials*, Elsevier, 2020, pp. 339–352.
- [11] A. Dhakshinamoorthy, A.M. Asiri, H. Garcia, 2D metal-organic frameworks as multifunctional materials in heterogeneous catalysis and electro/photocatalysis, *Adv. Mater.* 31 (2019), 1900617.
- [12] N.I. Gumerova, A. Rompel, Synthesis, structures and applications of electron-rich polyoxometalates, *Nat. Rev. Chem.* 2 (2018) 0112.
- [13] P. Mialane, C. Mellot-Draznieks, P. Gairola, M. Duguet, Y. Benseghir, O. Oms, A. Dolbecq, Heterogenisation of polyoxometalates and other metal-based complexes in metal-organic frameworks: from synthesis to characterisation and applications in catalysis, *Chem. Soc. Rev.* 50 (2021) 6152–6220.
- [14] C.T. Buru, O.K. Farha, Strategies for incorporating catalytically active polyoxometalates in metal-organic frameworks for organic transformations, *ACS Appl. Mater. Interfaces* 12 (2020) 5345–5360.
- [15] D.-Y. Du, J.-S. Qin, S.-L. Li, Z.-M. Su, Y.-Q. Lan, Recent advances in porous polyoxometalate-based metal-organic framework materials, *Chem. Soc. Rev.* 43 (2014) 4615–4632.
- [16] W. Xie, F. Wan, Immobilization of polyoxometalate-based sulfonated ionic liquids on UiO-66-2COOH metal-organic frameworks for biodiesel production via one-pot transesterification-esterification of acidic vegetable oils, *Chem. Eng. J.* 365 (2019) 40–50.
- [17] W. Xie, F. Wan, Biodiesel production from acidic oils using polyoxometalate-based sulfonated ionic liquids functionalized metal-organic frameworks, *Catal. Lett.* 149 (2019) 2916–2929.
- [18] W. Xie, C. Gao, J. Li, Sustainable biodiesel production from low-quantity oils utilizing H₆PV₃MoW₈O₄₀ supported on magnetic Fe₃O₄/ZIF-8 composites, *Renew. Energy* 168 (2021) 927–937.
- [19] J. Sun, S. Abednatanzi, P. Van Der Voort, Y.-Y. Liu, K. Leus, POM@MOF hybrids: synthesis and applications, *Catalysts* 10 (2020) 578.
- [20] L. Bromberg, Y. Diao, H. Wu, S.A. Speakman, T.A. Hatton, Chromium(III) Terephthalate Metal Organic Framework (MIL-101): HF-Free Synthesis, Structure, Polyoxometalate Composites, and Catalytic Properties, *Chem. Mater.* 24 (2012) 1664–1675.
- [21] J. Juan-Alcañiz, E.V. Ramos-Fernandez, U. Lafont, J. Gascon, F. Kapteijn, Building MOF bottles around phosphotungstic acid ships: one-pot synthesis of bi-functional polyoxometalate-MIL-101 catalysts, *J. Catal.* 269 (2010) 229–241.
- [22] L. Bromberg, T.A. Hatton, Aldehyde-alcohol reactions catalyzed under mild conditions by chromium(III) terephthalate metal organic framework (MIL-101) and phosphotungstic acid composites, *ACS Appl. Mater. Interfaces* 3 (2011) 4756–4764.
- [23] C.T. Buru, P. Li, B.L. Mehdi, A. Dohnalkova, A.E. Platero-Prats, N.D. Browning, K. W. Chapman, J.T. Hupp, O.K. Farha, Adsorption of a catalytically accessible polyoxometalate in a mesoporous channel-type metal-organic framework, *Chem. Mater.* 29 (2017) 5174–5181.
- [24] Z. Deng, C. Fang, X. Ma, X. Li, Y.-J. Zeng, X. Peng, One stone two birds: Zr-Fc metal-organic framework nanosheet for synergistic photothermal and chemodynamic cancer therapy, *ACS Appl. Mater. Interfaces* 12 (2020) 20321–20330.
- [25] Z. Fang, Z. Deng, X. Wan, Z. Li, X. Ma, S. Hussain, Z. Ye, X. Peng, Keggin-type polyoxometalates molecularly loaded in Zr-ferrocene metal organic framework nanosheets for solar-driven CO₂ cycloaddition, *Appl. Catal. B* 296 (2021), 120329.
- [26] A. Velená, N. Zarkovic, K. Gall Troselj, E. Bisenieks, A. Krauze, J. Poikans, G. Duburs, 1,4-dihydropyridine derivatives: dihydronicotinamide analogues—model compounds targeting oxidative stress, *Oxid. Med. Cell. Longev.* 2016 (2016), 1892412.
- [27] M.-L. Tîntaş, R. Azzouz, L. Peauger, V. Gembus, E. Petit, L. Bailly, C. Papamicaël, V. Levacher, Access to highly enantioenriched donepezil-like 1,4-dihydropyridines as promising anti-alzheimer prodrug candidates via enantioselective tsuji allylation and organocatalytic aza-ene-type domino reactions, *J. Org. Chem.* 83 (2018) 10231–10240.

- [28] V. Calvino-Casilda, R.M. Martín-Aranda, Ordered mesoporous molecular sieves as active catalysts for the synthesis of 1,4-dihydropyridine derivatives, *Catal. Today* 354 (2020) 44–50.
- [29] M. Nasr-Esfahani, S.J. Hoseini, M. Montazerzohori, R. Mehrabi, H. Nasrabadi, Magnetic Fe₃O₄ nanoparticles: efficient and recoverable nanocatalyst for the synthesis of polyhydroquinolines and Hantzsch 1,4-dihydropyridines under solvent-free conditions, *J. Mol. Catal. A Chem.* 382 (2014) 99–105.
- [30] R.H. Boecker, F.P. Guengerich, Oxidation of 4-aryl- and 4-alkyl-substituted 2,6-dimethyl-3,5-bis(alkoxycarbonyl)-1,4-dihydropyridines by human liver microsomes and immunochemical evidence for the involvement of a form of cytochrome P-450, *J. Med. Chem.* 29 (1986) 1596–1603.
- [31] F.P. Guengerich, W.R. Brian, M. Iwasaki, M.A. Sari, C. Baeaeerhielm, P. Berntsson, Oxidation of dihydropyridine calcium channel blockers and analogs by human liver cytochrome P-450 IIIA4, *J. Med. Chem.* 34 (1991) 1838–1844.
- [32] M.C. Bagley, M.C. Lubinu, Microwave-assisted oxidative aromatization of hantzsch 1,4-dihydro-pyridines using manganese dioxide, *Synthesis* 2006 (2006) 1283–1288.
- [33] J.R. Pfister, Rapid, high-yield oxidation of hantzsch-type 1,4-dihydropyridines with ceric ammonium nitrate, *Synthesis* 1990 (1990) 689–690.
- [34] J.-J. Vanden Eynde, A. Mayence, A. Maquestiau, A novel application of the oxidizing properties of pyridinium chlorochromate: aromatization of Hantzsch 1,4-dihydropyridines, *Tetrahedron* 48 (1992) 463–468.
- [35] N. Nakamichi, Y. Kawashita, M. Hayashi, Oxidative aromatization of 1,3,5-trisubstituted pyrazolines and hantzsch 1,4-dihydropyridines by Pd/C in acetic acid, *Org. Lett.* 4 (2002) 3955–3957.
- [36] B. Han, Z. Liu, Q. Liu, L. Yang, Z.-L. Liu, W. Yu, An efficient aerobic oxidative aromatization of Hantzsch 1,4-dihydropyridines and 1,3,5-trisubstituted pyrazolines, *Tetrahedron* 62 (2006) 2492–2496.
- [37] P.P. Ghosh, P. Mukherjee, A.R. Das, Triton-X-100 catalyzed synthesis of 1,4-dihydropyridines and their aromatization to pyridines and a new one pot synthesis of pyridines using visible light in aqueous media, *RSC Adv.* 3 (2013) 8220–8226.
- [38] H.T. Abdel-Mohsen, J. Conrad, U. Beifuss, Laccase-catalyzed oxidation of Hantzsch 1,4-dihydropyridines to pyridines and a new one pot synthesis of pyridines, *Green Chem.* 14 (2012) 2686–2690.
- [39] P. Prakash, E. Gravel, H. Li, F. Miserque, A. Habert, M. den Hertog, W.L. Ling, I.N. N. Namboothiri, E. Doris, Direct and co-catalytic oxidative aromatization of 1,4-dihydropyridines and related substrates using gold nanoparticles supported on carbon nanotubes, *Catal. Sci. Technol.* 6 (2016) 6476–6479.
- [40] Y. Liu, S.-Y. Moon, J.T. Hupp, O.K. Farha, Dual-function metal–organic framework as a versatile catalyst for detoxifying chemical warfare agent simulants, *ACS Nano* 9 (2015) 12358–12364.
- [41] D. Feng, Z.-Y. Gu, J.-R. Li, H.-L. Jiang, Z. Wei, H.-C. Zhou, Zirconium-metalloporphyrin PCN-222: mesoporous metal–organic frameworks with ultrahigh stability as biomimetic catalysts, *Angew. Chem. Int. Ed.* 51 (2012) 10307–10310.
- [42] Y.-Z. Chen, Z.U. Wang, H. Wang, J. Lu, S.-H. Yu, H.-L. Jiang, Singlet oxygen-engaged selective photo-oxidation over pt nanocrystals/porphyrinic mof: the roles of photothermal effect and pt electronic state, *J. Am. Chem. Soc.* 139 (2017) 2035–2044.
- [43] D. Han, Y. Han, J. Li, X. Liu, K.W.K. Yeung, Y. Zheng, Z. Cui, X. Yang, Y. Liang, Z. Li, S. Zhu, X. Yuan, X. Feng, C. Yang, S. Wu, Enhanced photocatalytic activity and photothermal effects of cu-doped metal-organic frameworks for rapid treatment of bacteria-infected wounds, *Appl. Catal. B* 261 (2020), 118248.
- [44] M.J. Katz, J.E. Mondloch, R.K. Totten, J.K. Park, S.T. Nguyen, O.K. Farha, J. T. Hupp, Simple and compelling biomimetic metal–organic framework catalyst for the degradation of nerve agent simulants, *Angew. Chem. Int. Ed.* 53 (2014) 497–501.
- [45] J. Wang, A.S. Cherevan, C. Hannecart, S. Naghdi, S.P. Nandan, T. Gupta, D. Eder, Ti-based MOFs: new insights on the impact of ligand composition and hole scavengers on stability, charge separation and photocatalytic hydrogen evolution, *Appl. Catal. B* 283 (2021), 119626.
- [46] S. Oudi, A.R. Oveisi, S. Daliran, M. Khajeh, R. Luque, U. Sen, H. García, Straightforward synthesis of a porous chromium-based porphyrinic metal-organic framework for visible-light triggered selective aerobic oxidation of benzyl alcohol to benzaldehyde, *Appl. Catal. A* 611 (2021), 117965.
- [47] C.-Y. Sun, S.-X. Liu, D.-D. Liang, K.-Z. Shao, Y.-H. Ren, Z.-M. Su, Highly stable crystalline catalysts based on a microporous metal–organic framework and polyoxometalates, *J. Am. Chem. Soc.* 131 (2009) 1883–1888.
- [48] M. Silva, A. Cardoso, F.D.L. Menezes, A.M.D. Andrade, M. Terrones, Heterogeneous Catalysts Based on H₃PW₁₂O₄₀ Heteropolyacid for Free Fatty Acids Esterification, *Biodiesel-Feedstocks and Processing Technologies*, 2011.
- [49] Y. Zhang, C. Huang, L. Mi, Metal–organic frameworks as acid- and/or base-functionalized catalysts for tandem reactions, *Dalton Trans.* 49 (2020) 14723–14730.
- [50] A. Modak, J. Mondal, A. Bhaumik, Porphyrin based porous organic polymer as bi-functional catalyst for selective oxidation and Knoevenagel condensation reactions, *Appl. Catal. A* 459 (2013) 41–51.
- [51] M. Safaiee, B. Ebrahimghasri, M.A. Zolfigol, S. Bagheri, A. Khoshnood, D. A. Alonso, Synthesis and application of chitosan supported vanadium oxo in the synthesis of 1,4-dihydropyridines and 2,4,6-triarylpyridines via anomeric based oxidation, *N. J. Chem.* 42 (2018) 12539–12548.
- [52] T. Toyao, N. Ueno, K. Miyahara, Y. Matsui, T.-H. Kim, Y. Horiuchi, H. Ikeda, M. Matsuoka, Visible-light, photoredox catalyzed, oxidative hydroxylation of arylboronic acids using a metal–organic framework containing tetrakis (carboxyphenyl)porphyrin groups, *Chem. Commun.* 51 (2015) 16103–16106.